

Biomass Ashes as Potential Raw Materials for Mineral Wool Manufacture: Initial Studies of Glass Structure and Chemistry

BACKHOUSE, Daniel, GUILBOT, Adrien, SCRIMSHIRE, Alex, EALES, James, DENG, Wei, BELL, Anthony, KABIR, Feroz, MARSHALL, Martyn, IRESOON, Robert and BINGHAM, Paul <<http://orcid.org/0000-0001-6017-0798>>

Available from Sheffield Hallam University Research Archive (SHURA) at:
<https://shura.shu.ac.uk/29342/>

This document is the Accepted Version [AM]

Citation:

BACKHOUSE, Daniel, GUILBOT, Adrien, SCRIMSHIRE, Alex, EALES, James, DENG, Wei, BELL, Anthony, KABIR, Feroz, MARSHALL, Martyn, IRESOON, Robert and BINGHAM, Paul (2022). Biomass Ashes as Potential Raw Materials for Mineral Wool Manufacture: Initial Studies of Glass Structure and Chemistry. *European Journal of Glass Science and Technology Part A Glass Technology*, 63 (1), 19-32. [Article]

Copyright and re-use policy

See <http://shura.shu.ac.uk/information.html>

Biomass Ashes as Potential Raw Materials for Mineral Wool Manufacture: Initial Studies of Glass Structure and Chemistry

Daniel J. Backhouse^{1,*}, Adrien Guilbot², Alex Scrimshire¹, James D. Eales¹, Wei Deng¹, Anthony M. T. Bell¹, Feroz Kabir¹, Martyn Marshall³, Robert Ireson^{3,4} and Paul A. Bingham¹

¹*Materials and Engineering Research Institute, College of Business, Technology and Engineering, Sheffield Hallam University, City Campus, Sheffield S1 1WB, UK*

²*Université de Rouen Normandie, 76130 Mont-Saint-Aignan, France.*

³*Glass Technology Services Ltd., Chapeltown, Sheffield S35 2PY, UK*

⁴*Glass Futures Ltd., Chapeltown, Sheffield S35 2PY, UK*

* Corresponding author email p.a.bingham@shu.ac.uk

Abstract

The energy-intensive and CO₂-generating nature of commercial mineral wool and glass production necessitates advances and changes in materials and processes. The derivation of raw materials from waste products arising from biomass energy generation offers the possibility of a two-fold environmental benefit: partial replacement of carbonate raw minerals in production, leading to lower CO₂ release during melting; and the utilisation and valorisation of by-products which may otherwise be landfilled. Glass samples with a basaltic mineral wool composition were produced with additions to the raw materials of 0, 1, 5 and 10 wt.% of a fly ash and a bottom ash arising from biomass combustion. The resulting glasses were analysed by X-Ray Fluorescence (XRF), X-Ray Diffraction (XRD), Dilatometry, ⁵⁷Fe Mössbauer and Raman spectroscopies, and their densities, molar volumes and viscosity-temperature profiles were calculated and compared against benchmark glass samples. All biomass ash-containing glasses were closely similar in both composition and properties to the benchmark glass, with up to 10 wt.% ash additions to the raw materials. In addition, the use of the biomass fly ash led to a reduction in batch CO₂ content estimated to be 1.5 kg CO₂ per tonne of batch for each 1 wt.% addition. These initial results provide evidence supporting the further development of these ash materials as potential value-added raw materials for mineral wool manufacture.

1. Introduction

In 2007, the European (EU27) commercial glass industry consumed approximately 98 TWh of energy, and generated around 28 MT of CO₂, equivalent to approximately 2% of regional CO₂ emissions.¹ More recent data for the EU27 glass industry does not exist in any single published study, however, recently Zier *et al.*² summarised in detail the more recent European and global glass industry data that is available, and provided thorough discussion of some of the decarbonisation opportunities available to the glass industry. In the UK, commercial glass production consumes ~6.5 TWh of energy per year and is responsible for an estimated 0.5 % of UK CO₂ emissions (2.2 MT).^{3,4} It is estimated that ~18% of CO₂ emissions from commercial glassmaking originate from the decomposition of carbonate raw materials such as limestone (CaCO₃) and soda ash (Na₂CO₃).⁴ Given the global drive towards decarbonisation, including decarbonisation of the glass industry^{2,4}, there is great value in investigating alternative raw materials with lower environmental impact.

Although not always considered a ‘glass’ product,¹ mineral wool (specifically stone/rock wool) is a glassy material generated by melting raw materials at high temperatures, and, as such, has many of the same issues regarding CO₂ release as traditional commercial glass products such as soda-lime-silica container, flat or fibre glasses. Production of mineral wool has been estimated to be approximately 2.0 – 2.5 MT per year in the EU.^{5,6} Minerals, primarily basalt, and other raw materials are mixed and then melted together inside a modified blast furnace to produce a molten oxide slag. The (glass-forming) molten oxide slag is then poured onto rapidly rotating wheels which cause the formation of long filaments or fibres as the melt is spun from the surface of the wheels, and rapidly cooled to form the glass filaments. These filaments or fibres are collected together into mats and coated with an organic binder, forming the mineral wool insulation material.⁷

Biomass combustion is a rapidly growing source of renewable electricity, with worldwide biomass electricity generation having increased by over 260 % between 2000 and 2017.⁸ Biomass refers to plant and animal matter that is used for energy generation, or as raw materials in industrial processes, and includes materials such as wood, grass, straw, agricultural wastes from harvesting/farming, and residues from industrial food production. Perennial plants regularly used for biomass power, such as *Miscanthus x giganteus*, sequester CO₂ in their root systems during growth which opens up the possibility of carbon-neutral energy generation.⁹ The biomass combustion process generates significant quantities of ash (an estimated 480 MT per year worldwide), the majority of which is disposed of by landfill.^{9,10} Waste materials being disposed of in this manner have a significant and detrimental effect on the environmental credentials of biomass energy generation. However, biomass ashes are known to contain elements, e.g. Si, Al, Na, K, Ca, Mg, P, which have potential value in other industries, including construction, glass and ceramic manufacture, chemical manufacture and agriculture.¹¹ Therefore a wide variety of research has been undertaken in attempts to valorise biomass ashes for a range of industrial applications.^{11–17} There exists a strong synergy between the search for alternative raw materials for glass production and the drive towards valorisation of biomass ashes. As products of combustion, not only do the biomass ashes contain elements of relevance to glass production (e.g. Si, Al, K, Ca), but they are also significantly decarbonised compared to standard glass raw materials (e.g. CaCO₃, Na₂CO₃). Hence, there is the possibility of two-fold environmental benefit through use of biomass ashes in glass production: (i) reduction in biomass ash material going to landfill; and (ii) reduction in the CO₂ released to the atmosphere during glass production.

There is a long and established history of the use of biomass ashes in the production of glass. Silicate glasses require fluxes, typically alkali or alkaline earth oxides, in order to reduce the melting temperature of SiO₂ to values which can be economically achieved

through the use of contemporary furnace technologies. For centuries and even millennia, plant ashes were used as primary sources of alkali and alkaline earth oxide fluxes. Plant ashes are known to have been used in glass and glaze production in Egypt (from 16th Century B.C.)¹⁸⁻²¹ and China (from 1700 B.C.)^{22,23}, as well as throughout Europe and the Islamic world for centuries (ca. 15th Century B.C. onwards)²⁴⁻²⁹. In addition, the use of wood ashes in glass-making was prevalent in northern and western Europe until the 18th – 19th Centuries A.D.³⁰⁻³² Over time, as the quality and consistency requirements of glass became tighter, biomass ashes were gradually replaced with mined and synthetic raw materials (e.g. limestone and soda ash) which can be produced with more tightly controlled compositions.³² However, biomass ashes in modern times are generally produced as part of carefully-controlled industrial combustion processes, which was not the case prior to the 20th Century A.D. This suggests that the compositional variability of modern biomass ashes may be significantly less than for historical biomass ashes and justifies further research in this field.

Mineral wool presents a potentially useful route for biomass ashes to be used in glass production for two primary reasons: firstly, mineral wool has less stringent requirements on colour (which is primarily dictated by the transition metal content of the raw materials, e.g. Fe) compared to float and container glasses; and, secondly, industrial waste materials, including ash materials, are already used in the manufacture of mineral wool, e.g. slag material from steel and other metal production, coal fly ash,³³⁻³⁶ thereby establishing precedence and evidencing the experience within this industry of handling such raw materials.

In order to investigate the feasibility of introducing biomass ashes as raw materials for the production of mineral wool, two series of laboratory-produced representative mineral wool glass samples were produced using a biomass fly ash (BFA) and a biomass bottom ash (BBA). The properties (chemical composition, crystallinity, density, redox and structure) of these samples were measured and compared against a benchmark glass representative of

current commercial mineral wool raw materials and glass compositions, and the effects of biomass ash additions on total batched CO₂ were also calculated.

2. Experimental Procedures

2.1 Sample Preparation

Eight representative mineral wool (MW) glass samples were produced for this investigation: two benchmark glasses, MW and MW-C; and six glasses containing 1, 5 and 10 wt.% of either biomass fly ash (FA- x) or biomass bottom ash (BA- x), where x denotes the biomass ash content in wt.%. The MW-C benchmark contains the same raw material proportions as MW, but with 5 wt.% of the batch replaced with coke. For each sample, 50 g batches were produced utilising appropriate amounts of the following industrial reagents: basalt, blast furnace slag (BFS), steel slag, dolomite, coke, biomass fly ash (BFA) and biomass bottom ash (BBA). The batch compositions of these samples are shown in Table 1, and their analysed compositions (determined by X-Ray Fluorescence (XRF) spectroscopy) are shown in Table 2 (Section 3.1). Coke was not included as it primarily consists of C which cannot be detected by the available laboratory-scale instruments due to its low atomic mass. It should be noted that coke is the fuel used to heat the cupola furnaces used for mineral wool production, rather than an intrinsic component of the glass.⁶ However, it plays a strong role in determining redox conditions in the cupola furnace during melting, and hence it was included here in the MW-C sample to provide closer comparison between the melting conditions accessible in our laboratory and those present in cupola furnaces.

All reagents were milled for 1 minute at 700 rpm using stainless steel milling media in a Retsch RS200 vibratory disc mill, achieving a particle size of < 100 µm prior to batching. The basalt, blast furnace slag, steel slag, dolomite and coke were obtained from UK

commercial raw materials suppliers. The biomass fly and bottom ashes were obtained from UK biomass or co-combustion power plants. The fly ash was formed from the combustion of virgin wood, whereas the bottom ash was formed from the combustion of a mixture of waste wood, virgin wood and recycled fibre. The XRF-determined compositions of the ashes can be found in Table 3 (Section 3.1). Each 50 g batch was placed in a recrystallised Al₂O₃ crucible and then heated to 1450 °C at 10 °C/min in an electric furnace. The resulting melt was held at 1450 °C for 3 h before being poured into a steel mould, allowed to cool until sufficiently stiff, then removed from the mould and annealed in an electric furnace at 650 °C for 1 h, followed by cooling to room temperature at 1 °C/min. The annealing temperature was selected based on literature T_g values for glasses with similar compositions, with T_g's of 660 – 690 °C³⁶ and 680 °C³⁷.

2.2 X-Ray Fluorescence (XRF) Spectroscopy

Compositional analysis was performed using a PANalytical MagiX Pro XRF spectrometer equipped with a Rh anode X-ray tube. Fused beads were produced from approximately 1 g of powdered sample mixed with approximately 10 g of lithium tetraborate (Li₂B₄O₇) flux, which were then placed into a Claisse LeNeo fused bead maker to be melted at 1065 °C and then cast into a 5% Au – 95% Pt mould. The XRF spectra were analysed using a version of the OXI programme,³⁹ a Wide Range Oxide XRF programme developed and modified in-house. Details of the included oxides and calibration ranges can be found in Bell *et al.*⁴⁰ Uncertainties associated with each measurement were estimated to be related to the maximum of the relative standard deviation of triplicate measurements of a standard reference material analysed using the same instrument and software.⁴⁰ Based on these values, oxides present in amounts > 10 wt.% have a Relative Standard Deviation (RSD) of ~0.2 %, oxides present in amounts between 1 and 10 wt. % have an RSD of ~ 1 %, oxides between

0.1 and 1 wt.% have an RSD of 5 %, and oxides present below 0.1 wt% have an RSD of 10 %.

2.3 X-Ray Diffraction (XRD)

X-Ray Powder Diffraction was performed on powdered sections of each sample. All data was collected using a Philips X'Pert Pro X-Ray diffractometer with a Cu K α source ($\lambda = 1.5406$ Å), operating in Bragg-Brentano geometry. The operating voltage was 40 kV and the operating current was 40 mA. Powdered samples were placed on a spinner stage rotating at 15 rpm, with diffraction patterns collected over a 2θ range of 5 - 80 ° with a step size of 0.013 ° 2θ .

2.4 Carbon Elemental Assay

The BFA and BBA were analysed to determine their carbon content. The analyses were performed at a testing facility with ISO 17025 (UKAS) accreditation, utilising a LECO CS448ES combustion furnace. The ash samples were milled at 700 rpm for one minute, using stainless steel media in a Retsch RS200 vibratory disc mill, prior to combustion. Combustion occurred in a high frequency induction furnace under a pure O₂ atmosphere to ensure complete combustion. The furnace was calibrated with appropriate Certified Reference Materials (CRMs), with the range of calibrations covering both the samples analysed. Carbon detection was through infra-red (IR) spectroscopy. The measurement uncertainties, as a percentage of the measured value were: 2 % over 3 wt.% C and 5 % over 0.2 wt.% C. The detection limit was < 10 ppm.

2.5 Density and Molar Volume

The densities of the samples were measured using the Archimedes method, with distilled water as the suspension medium. Densities were calculated using:

$$\rho = \left(\frac{W_A}{W_A - W_W} \right) \delta_W \quad (1)$$

Where: ρ is the density in g/cm^3 ; W_A and W_W are the weights of the sample in air and water, respectively; and δ_W is the density of the distilled water (corrected for temperature). Monolithic samples greater than 10 g in mass were used. Triplicate data were collected and the average value obtained. A correction was applied to the data to account for the variation of the density of water with temperature. The uncertainties correspond to the standard deviation of the triplicate measurements.

The molar volume, V_m , of each sample was calculated from their analysed chemical compositions and densities, ρ , by:

$$V_m = \frac{\bar{M}}{\rho} \quad (2)$$

where \bar{M} is the average molar volume, calculated by:

$$\bar{M} = \sum_i x_i M_i \quad (3)$$

where: x_i is the molar fraction of each oxide, i ; and M_i is the molecular mass of each oxide. Uncertainties on the molar volumes are conservatively estimated at 5 % due to the number of different variables through which the uncertainties are introduced.

2.6 Raman Spectroscopy

A monolith of each sample was sectioned to have two parallel faces using a precision saw with diamond blade. The top face was then ground to a P1200 finish using SiC grit paper. Raman spectra were collected using a Thermo Scientific DXR2 spectrometer with a depolarised, 10 mW, 532 nm laser, between 50 and 2000 cm^{-1} . The Raman spectra were corrected for temperature and excitation line effects using the approach developed by Shuker & Gammon⁴¹ and Galeener & Sen⁴², as given by Le Losq *et al.*⁴³:

$$I = I_{Obs}[\nu_0^3[1 - \exp(-h\nu/kT)]\nu/(\nu_0 - \nu)^4] \quad (4)$$

where I is the corrected Raman intensity; I_{Obs} is the observed Raman intensity; ν_0 is the wavenumber of the incident laser light (18796.99 cm^{-1} for 532 nm laser light); h is Planck's constant (6.62604×10^{-34} J s); c is the speed of light (2.9979×10^{10} m s^{-1}); k is Boltzmann's constant (1.38066×10^{-23} J K^{-1}); T is the absolute temperature in K; and ν is the Raman shift in cm^{-1} . This treatment of Raman spectra is commonly referred to as 'Long Correction' after the description by Long⁴⁴.

2.7 ⁵⁷Fe Mössbauer Spectroscopy

Transmission ⁵⁷Fe Mössbauer spectroscopy measurements were carried out over a velocity range of ± 4 mm s^{-1} , at room temperature, using a constant acceleration spectrometer with a 25 mCi ⁵⁷Co(Rh) source. The data were fitted using Lorentzian line shapes in the *Recoil* software package and were calibrated against thin α -Fe foil.⁴⁵ The data were fitted using a combination of Fe^{3+} and Fe^{2+} paramagnetic doublets, assigned in agreement with existing literature for iron in silicate glasses.⁴⁶⁻⁴⁸

2.8 Dilatometry

Dilatometry was performed on all samples using a calibrated Netzch DIL-402PC dilatometer. Coefficients of thermal expansion (α), dilatometric softening points (T_d) and glass transition temperatures (T_g) were measured using a connected computer, with a heating rate of 10 °C/min and a constant applied force of 600 mN. Thermal expansion coefficients apply to the region 50 – 300 °C.

2.9 High-Temperature Viscosity Modelling

The high-temperature viscosity of each of the samples was modelled using the Slag Viscosity Database (SVD) and Slag Viscosity Predictor (SVP) tools developed by Duchesne *et al.*⁴⁹ The SVD tool was used to evaluate which viscosity models would be most applicable to the samples in this work. The database was searched to find the most similar compositions to the samples here, and the viscosity models with the lowest average absolute logarithmic errors (AALE) for these data were selected for modelling using the SVP tool. The four selected models were: the S^2 model⁵⁰; the Watt-Fereday model⁵¹; the Shaw model⁵²; and the BBHLW model⁵³. Melting point ($\log(\eta/\text{dPa}\cdot\text{s}) = 2$), fibre-forming temperature ($\log(\eta/\text{dPa}\cdot\text{s}) = 4$) and glass transition temperature ($\log(\eta/\text{dPa}\cdot\text{s}) = 12$, Watt-Fereday model only) values were extracted from the models for each sample. Uncertainties for each model are based on their Average Absolute Logarithmic Error (AALE):

$$AALE = \frac{1}{N} \sum_{i=1}^N |\log_{10}(p_i) - \log_{10}(m_i)| \quad (5)$$

where p_i is the i^{th} predicted value and m_i is the i^{th} measured value for N data points.⁵⁴ All AALE values quoted are based on the calculations of Duchesne *et al.* from the ‘2C’ case

study,⁴⁹ and are: S^2 AALE = 0.27; Watt-Fereday AALE = 0.33; Shaw AALE = 0.55; and BBHLW AALE = 0.30.

3. Results

3.1 XRF Spectroscopy

The XRF data for the conventional raw materials and biomass ashes can be seen in Tables 2 and 3, respectively. The biomass ashes provide many of the same major oxides as the conventional raw materials, such as Al_2O_3 , SiO_2 , CaO and Fe_2O_3 . Table 4 shows the XRF-determined compositions of the samples, in weight percent, in addition to the bulk density and molar volume of each sample. The mean and standard deviation (σ) for the major oxides (> 1 wt.%) across every sample are displayed in Table 5. The relative standard deviation (RSD) was 5.42 % for MgO , with all other values (with the exception of Al_2O_3 (5.16 %)) less than 3.5 %.

3.2 X-Ray Diffraction (XRD)

Figure 1 shows the diffractograms for each sample. Each diffractogram exhibits a region of diffuse scattering between ~ 21 and $38^\circ 2\theta$, with no sharp, intense peaks observed. This confirms that each of the samples is X-ray amorphous, with any crystalline content lower than the detection limit of the instrument. The diffuse scattering regions all occur in the same 2θ range with the same peak shape. This qualitatively suggests that the samples are structurally similar.

3.3 Raman Spectroscopy

The Long-corrected Raman spectra of the samples (Figure 2) are closely similar, within uncertainties, and all exhibit three primary regions: 400 – 630 cm^{-1} , 630 – 800 cm^{-1} and 800 – 1200 cm^{-1} . All three regions contain broad, convoluted features with significant overlap between regions. The feature in the 800 – 1200 cm^{-1} region has the greatest intensity, followed by the features at 630 – 800 cm^{-1} and 400 – 630 cm^{-1} , respectively. Figure 3 shows the difference plots of each sample compared to the MW benchmark, which were constructed by subtracting each sample's normalised spectrum from the normalised spectrum of the corresponding benchmark glass. These data confirm that any deviations from the benchmark spectrum are small and non-systematic. Given high-quality and well-separated spectral data, it is possible to deconvolute the 800 – 1200 cm^{-1} region to obtain the Q_n speciation of the sample. However, this is not possible for the collected spectra here due to the significant overlap between the 800 – 1200 cm^{-1} and 630 – 800 cm^{-1} contributions and, moreover, the presence of multiple elements capable of contributing to the Q-species region (Si, Al, Fe).

3.4. ^{57}Fe Mössbauer Spectroscopy

The ^{57}Fe Mössbauer spectra and fitting parameters for the spectra obtained for the MW, MW-C, FA-10 and BA-10 samples are displayed in Figure 4 and Table 6, respectively. Each spectrum was fitted using three Lorentzian paramagnetic doublet components; two Fe(III) and one Fe(II), in accordance with existing literature regarding Mössbauer analysis of silicate glasses.^{46,47,55} Here, the Fe(III) doublet of each spectral fit with the larger quadrupole splitting (QS) is defined as octahedrally co-ordinated, and the doublet fit with the smaller values as tetrahedrally co-ordinated.^{48, 56-60} These configurations indicate the iron occupying a network-modifying role and network-forming role, respectively.

In the absence of recoil-free fractions for the iron environments observed in these materials, which would require many additional measurements to establish, it is not possible

to be fully quantitative in terms of redox analyses, however, robust qualitative comparison can be made between spectra. Most notably among the spectra reported here is the significant increase in Fe(II) identified in sample MW-C, and to a smaller extent in sample FA-10, relative to the other two spectra, as highlighted in their relative areas in Table 4. The increased abundance of a reduced iron phase (Fe^{2+}) is consistent with expectations with regards to sample MW-C, as the addition of coke to the raw materials will yield more reducing melting conditions, causing reduction of some of the iron in the melt from Fe^{3+} to Fe^{2+} and thereby affecting the $\text{Fe}^{2+}/\Sigma\text{Fe}$ ratio of the resulting glasses. The increase in Fe^{2+} content in sample FA-10 suggests that the fly ash contains a greater proportion of reducing components (carbon) than the bottom ash.

3.5 Batch CO_2 Analysis

As discussed in Section 1, raw materials are responsible for a significant fraction of the CO_2 release during glass production. By considering the changes in batch composition with the addition of ash, the total batched CO_2 can be estimated for each sample. The total CO_2 content of each 50 g batch, B_{CO_2} , can be estimated by:

$$B_{\text{CO}_2} = \sum_i (m_{\text{CO}_2,i} \times m_i) \quad (6)$$

where: $m_{\text{CO}_2,i}$ is the mass fraction of CO_2 in the batch material, i ; and m_i is the mass of raw material in the batch. Although the biomass ashes do contain carbon, this carbon is likely to be organic in nature, and therefore reduced, and so could be used to supplement the usual addition of coke to the mineral wool batch for manufacture. Therefore, the addition of ash can be held to be carbon-neutral, given adequate reformulation. Table 7 shows the estimated batched CO_2 values for all samples, as well as the equivalent kg of CO_2 per tonne of batch

values. Data are not presented for sample MW-C given that this sample was produced using coke, and so is not directly comparable to the other samples, which were produced without coke.

The addition of BFA to the batch, and corresponding reformulation, led to a noticeable decrease in batch CO₂ content, equivalent to approximately 1.5 kg of CO₂ per tonne of batch for every 1 wt% of ash added. Conversely, the addition of BBA led to an increase in batched CO₂ content, equivalent to around 3.8 kg of CO₂ per tonne of batch for every 1 wt% of ash added. This discrepancy can be understood by considering the purpose of dolomite and the chemical compositions of the ashes. Dolomite is included in the batch to provide Ca and Mg to the glass. The BFA contains Ca and Mg and therefore the amount of dolomite required can be reduced.

In mineral wool production, the use of coke as the fuel within the cupola has a significant impact on the overall CO₂ release during the process. An estimate of the CO₂ release from coke combustion can be calculated from the mass of coke, m_C , and the specific CO₂ content of the coke, c_C . Assuming a coke content of 130 kg for every tonne of batch and a c_C value of 2.82 kg CO₂ kg⁻¹ coke gives a value of 366.6 kg of CO₂ generated per tonne of batch.

3.6 Dilatometry

The coefficient of thermal expansion (α), dilatometric softening point (T_d) and glass transition temperature (T_g) values for each sample are shown in Table 8, along with values for ΔT , where $\Delta T = T_d - T_g$. The α and T_g values for all samples appear to be equivalent within error. A small increase in T_d is observed with addition of BFA and BBA, with the effect greater for BFA. This resulted in larger ΔT values for the ash-containing samples compared to the benchmark MW sample, with an increase of up to 11 °C for the FA-x samples.

3.7 High-Temperature Viscosity Modelling

The viscosity modelling data (Table 9) showed significantly greater variation between different models than between the samples. For example, the range of modelled $\text{Log}(\eta/\text{dPa}\cdot\text{s}) = 2$ temperature values for MW across the four models is 122 °C, whereas the range across all samples using the S^2 model is 16 °C. Overall, the greatest variation between samples was 45 °C for the $\text{Log}(\eta/\text{dPa}\cdot\text{s}) = 2$ temperature values calculated by the Shaw model. Given the variation between models, this suggests that the viscosity-temperature relationships of all samples are closely similar. The FA-10 sample appears to be a relative outlier; when discounted, the maximum variation between samples reduces to 28 °C.

Glass transition temperatures were modelled using the Watt-Fereday model only, as it was the only model capable of reasonable modelling at such high viscosities. The Watt-Fereday model provided a reasonable prediction of the T_g values of these samples by comparison with the measured values, with experimental minus modelled values of 27 – 39 °C, equivalent to errors of 4.4 – 5.8 %.

4. Discussion

X-ray amorphous mineral wool glasses can be successfully melted at 1450 °C with up to 10 wt. % addition of biomass fly and bottom ashes. XRF spectroscopy showed consistency in the chemical compositions of the samples; the relative standard deviation (RSD) for the seven primary components (SiO_2 , CaO , Al_2O_3 , Fe_2O_3 , MgO , Na_2O , MnO_2) was within approximately 5 %, was less than 0.5 % for the density and under 0.7 % for the molar volume.

The Raman spectra collected on the mineral wool samples are noticeably similar to Raman spectra of a number of basaltic glasses in the literature.⁶¹⁻⁶⁵ The three regions of the spectra have been denoted in the literature as high-, mid- and low-wavenumber (HW, MW, LW),⁶² or

high-, middle- and low-frequency (HF, MF, LF).⁶⁴⁻⁶⁶ Depending on the intensity of the mid-wavenumber region, or the degree of convolution with the high-wavenumber region, the spectra can also be split into two regions: low-frequency/wavenumber and high frequency/wavenumber.^{56,58} The LW/LF region is generally reported between $\sim 200 \text{ cm}^{-1}$ and $\sim 650 \text{ cm}^{-1}$.^{57,60,61} The band in this region tends to be assigned to vibrations of bridging-oxygens forming rings with three or more SiO_4 tetrahedra.^{61,62,64-66} The MW/MF region is reported variously between 600 and 800 cm^{-1} ,⁶⁵ between 650 and 850 cm^{-1} ,⁶² or between 650 and 900 cm^{-1} .⁶⁶ This region is not always given a structural assignment,⁶² but there is a suggestion that it can be attributed to the inter-tetrahedral bending mode of polymerised species.⁶⁴ The HW/HF region is usually reported as an interval in the range of $800 - 1250 \text{ cm}^{-1}$.^{61,62,66-68} The firm consensus in the literature is that the band(s) in the HW/HF region correspond to the symmetric and asymmetric stretching modes of $\text{Q}_n \text{SiO}_4$ tetrahedra, where n is the number of bridging-oxygens.^{61,66-70} Given that this region gives information on the Q_n species in the glass, deconvolution of the band(s) can provide vital information on the structure and polymerisation of the glass network. However, due to the degree of convolution of the band, and the overlap with the band in the MW/MF region, combined with the presence of 3 cations capable of contributing Q_n species (Si, Al, Fe),⁷⁰ a deconvolution was not possible for these samples. In terms of qualitative assessment, the spectra are closely similar for all samples (c.f. Raman difference plots in Figure 3), confirming little difference in structure to complement the minor variations in chemical composition that have also been measured.

High-temperature viscosity modelling also shows minimal variation between the different samples. Viscosity is arguably the most important property of industrial glass melts. Any change in viscosity profile will affect: melting temperature, melting rates, melt homogeneity, corrosion of refractories, product formation, annealing temperature. It is thus vital to know

how any changes to the process (including batch changes) will affect the viscosity of the melt. However, experimental determination of high-temperature viscosity is difficult (due to the very low availability of testing facilities), time-consuming (it can take an entire day to accurately measure one sample) and expensive, and was not available to us during the present work. Computational modelling of viscosity is therefore a highly desirable technique, as has been fully validated and proven to be robust, e.g. by Lakatos et al.⁷¹⁻⁷³ and Mauro et al.⁷⁴. Given the great importance of viscosity in glass production, any viscosity model requires a high degree of accuracy and precision. Table 10 shows the viscosity data at 100 °C intervals for sample MW for each of the four models. Although the values are closely similar at the highest temperature (1500 °C), variation between them develops as the temperature decreases; at 1000 °C, the variation is greater than an order of magnitude, and by 600 °C there are large differences between the highest and lowest modelled viscosity values, showing that the most significant differences between models occur at relatively low temperatures / high viscosities. This is illustrated by the ability of the Watt-Fereday model to estimate T_g ($\text{Log}(\eta/\text{dPa}\cdot\text{s}) = 12$) values within 5 % of the measured value, whilst the other models considered do not provide estimates that would be considered reasonable. It is likely that the primary issue with these models is that they have not been developed using data from samples with similar compositions to those investigated here. The Slag Viscosity Database tool contained measured viscosity data for 3 glasses (slags) with similar chemical compositions to those studied here, encompassing 29 out of a total of over 4000 data.⁴⁹ Thus, one aspect of further work for developing biomass ash raw materials will be further confirming the modelled viscosities through experimental viscometry data. Crucially to the present study is our ability to show, through a combination of dilatometry measurements, viscosity modelling, XRF analyses and Raman spectroscopy, that all glasses studied here are

compositionally and structurally similar, and that they display closely similar viscosity-temperature behaviour to one another and to the benchmark samples.

The ^{57}Fe Mössbauer spectra show that the MW-C sample has increased Fe^{2+} content compared to the MW benchmark. This is due to the reducing action of the coke during melting. Although the primary purpose of the coke is as the fuel for the cupola furnace, the oxidative process of combustion leads to a corresponding reductive action on the other materials present in the furnace. It should be noted that the $\text{Fe}^{2+}/\Sigma\text{Fe}$ value for sample MW-C was 0.35, which is significantly lower than values for industrial materials found in literature (~ 0.97).⁷⁵ The reduced nature of mineral wool glass has been purported to be beneficial. The presence of higher levels of Fe^{2+} leads to the formation of a crystalline nanolayer on the surface of mineral wool fibres during heating in oxidising conditions.^{37,38,76} This crystalline nanolayer has a mitigating effect on the bulk crystallisation of the fibres, leading to significantly greater high-temperature stability, a valuable effect for a material used as insulation in construction, but not studied here since our initial focus was on bulk glasses and not on glass fibres or filaments. It should be noted that the FA-10 sample also exhibits a slight increase in Fe^{2+} compared to the benchmark MW sample ($\text{Fe}^{2+}/\Sigma\text{Fe} = 0.19$ and 0.15 , respectively). This is attributed to the residual carbon in the biomass ash which did not fully combust during power generation. The BFA and BBA samples were analysed for residual carbon content by combustion testing with infra-red detection; the BFA sample was found to have 6.26 wt. % residual carbon, whereas the value for the BBA sample was 0.24 wt. %. This residual carbon could be used in partial replacement for coke.

The Mössbauer data for samples MW-C and FA-10 may also explain the slightly lower Fe_2O_3 contents of these samples (11.46 and 11.39 wt. %, respectively, compared with 12.28 wt. % for sample MW). Reducing environments leading to the formation of Fe^{2+} often also lead to the formation of Fe^0 , that is, metallic Fe. Small amounts of metallic Fe were found at

the base of the crucibles used to melt the MW-C and FA-10 samples, after pouring. The metallic Fe was present as a single bead in each case. When the glass phases were analysed, therefore, it would be expected that the Fe_2O_3 content would be slightly decreased and this was supported by the XRF results.

The XRF analyses of the samples show that minor amounts of transition and heavy metals – Cr_2O_3 , MnO_2 , ZnO and BaO – are present in the benchmark glass sample. The Cr_2O_3 and MnO_2 arise primarily from the steel slag, whereas the ZnO and BaO arise from the basalt and blast furnace slag. In general, the ash-containing samples contain similar or lower amounts of heavy metals than the benchmark. The exceptions are: the BA-10 sample contains 0.05 wt.% ZnO compared to 0.02 wt.% for the benchmark; and the FA-1 and FA-10 samples contain BaO levels of 0.04 and 0.05 wt.%, respectively, compared to 0.02 wt.% for the benchmark. However, XRF analysis detected no Pb or Cd in any of the samples, which suggests that, if present, they are in concentrations of < 10 ppm. Despite the presence of measurable levels of ZnO or BaO in samples BA-10, FA-1 and FA-10, there are unlikely to be issues with such elements for these samples as mineral wool is not a food contact material and so there are not the same concerns on heavy metal migration from the glass.

Estimations of the CO_2 contents of the sample batches (Table 6), suggest that it is possible that the biomass ashes could be used to reduce the total batched CO_2 in mineral wool production. However, it must be stressed that these estimations require confirmation by experimental determination of CO_2 emissions from the different batches. The potential reductions in batch CO_2 content are also limited by current formulation of mineral wool batches. The primary contributor of batch CO_2 for these glasses is dolomite, which is used to provide CaO and MgO to the melt. The amount of dolomite required is governed by the required MgO content (and to a lesser extent CaO , which is also provided by blast furnace slag and steel slag). As a consistent chemical composition across all samples was targeted,

that meant that dolomite could only be decreased to the extent that MgO could be added through the biomass ash (biomass fly ash MgO content is 2.22 wt.%, biomass bottom ash MgO content is 1.52 wt.%). In order to obtain further CO₂ reductions, one of two paths must be followed (corresponding to principles 1 and 3 discussed by Bingham⁷⁷): (1) Reformulate the chemical composition of the mineral wool glass to reduce the MgO content, and hence the dolomite requirement; (3) find an alternative, low CO₂, source of MgO. Path 1 is outside the scope of this manuscript but would certainly be an interesting piece of research for the future. Currently, a biomass ash which would provide a significant amount of MgO so that Path 3 could be followed has not been identified. However, this is an area in which further research is being undertaken, and investigations are being extended to waste materials from other industries.

The CO₂ calculations were based on the CO₂ content of the batches, although, as mentioned above, there are other factors that must be taken into account, particularly the presence of coke as a fuel. The BFA material contains significant amounts of unburnt carbon which could potentially be used in partial substitution for coke. However, the relationship between increasing carbon through ash and decreasing coke content is unlikely to be 1:1. The heat capacity of different cokes is known to vary,⁵ so it is highly likely that the heat capacity of the residual carbon in the BFA will be different. In addition, the reactivity of the coke can have a significant effect on the amount required for mineral wool production.⁷⁸ Furthermore, the carbon content of the BFA is likely to vary from batch to batch, which would complicate its ability to substitute for coke. The extent to which the BFA could be used in partial substitution for coke in mineral wool production would therefore require further detailed investigation of its heat capacity and reactivity, as well as analysis of the variability of the carbon content of the ash.

When considering new raw materials for use in mineral wool manufacture, the consistency of the proposed raw material, in terms of time and source, is vital. If there is significant variation in the chemical composition of the material over time, the production process becomes complex, with the batch recipe requiring alteration with each new delivery of material. In order to assess the variability of the BFA material, 17 samples were taken from a UK biomass power plant over a period of approximately 13 months, with their chemical compositions analysed by XRF. A summary of the data is given in Table 11. For the 5 primary oxides (SiO_2 , CaO , Al_2O_3 , K_2O and Fe_2O_3), the relative standard deviation values ranged from 4.59 % (Fe_2O_3) to 10.15 % (CaO). If the potential absolute change in each oxide, assuming BFA were 10 wt.% of the batch, is considered (equal to the value range of each oxide divided by 10), it suggests that the maximum possible batch-to-batch variation in the five primary oxides would be 0.91 % (SiO_2), 0.77 % (CaO), 0.45 % (Al_2O_3), 0.43 % (K_2O) and 0.18 % (Fe_2O_3). These values are consistent with similar levels of variability in the existing raw materials used in mineral wool production (e.g. blast furnace slag^{79,80}) and could be further improved through processing of the biomass ash materials, such as magnetic separation,⁸⁰ or through on-site blending techniques, such as are common in many foundation industries.⁸² Overall this provides confidence in the potential suitability of such biomass ashes as those studied here for application as replacement, value-added raw materials in future mineral wool manufacture. However, certain components of the BFA and BBA materials studied here (Table 3), in particular Cl, can lead to environmental issues when emitted from high temperature processes such as mineral wool manufacture. As a result of its potentially harmful nature, atmospheric emissions of Cl and HCl are regulated in many countries, and they are controlled by standard atmospheric control media including electrostatic precipitators, filters, cyclones, where these off-gases and particulates are captured^{83,84} and their acidity is neutralised through addition of appropriate alkali media.

Consequently, given the very low concentrations of Cl in the BFA and BBA by-products studied here, it is not envisaged that these are likely to cause problems for current abatement technologies installed at mineral wool manufacturing sites, however, further research would enable this to be confirmed and quantified.

5. Conclusions

Two different types of biomass ash, fly and bottom, have been added to mineral wool batch up to 10 wt.% loading to produce X-Ray amorphous glasses with only minor deviations from the ash-free benchmark in chemical composition and structure. XRF analyses of the ash-containing mineral wool samples suggest that only low levels (< 10 ppm) of heavy metals such as Pb and Cd are present. Raman spectra show that the samples are close in structure to natural basaltic glasses, consistent with batch compositions with 50 – 60 wt.% basalt. Viscosity modelling using a tool developed for slag materials suggests that the addition of the biomass ashes is unlikely to have a significant effect on melt ($\text{Log}(\eta/\text{dPa}\cdot\text{s}) = 2$) and fibre-forming ($\text{Log}(\eta/\text{dPa}\cdot\text{s}) = 4$) viscosities.

The biomass fly ash shows promise as its addition led to a reduction in the dolomite required in the batch and therefore to an estimated reduction in the total batched CO_2 . These estimates require confirmation by experimental means, however. In addition, ^{57}Fe Mössbauer spectroscopy showed that the ash has a reducing effect on the Fe in the glass, raising the possibility that residual carbon in the fly ash could be used in partial replacement for coke.

In order to further understand the feasibility of using biomass ashes for mineral wool manufacture, investigation is required into their thermal properties (e.g. energy requirement for decomposition and melting, reaction behaviour with other raw materials), as well as an experimental determination of the effect of the ash on key processing parameters, such as the

viscosity in the melting and forming ranges, and crystallisation behaviour. Qualification of vital product properties, e.g. chemical durability, is also required. However, this initial investigation demonstrates that there is value in undertaking further research into the use of biomass ashes as raw materials for mineral wool production.

Acknowledgements

The authors would like to acknowledge financial support from Innovate UK under grant number 104382; and from BEIS under project number EEF6023.

References

1. Schmitz, A., Kamiński, J., Maria Scalet, B. & Soria, A. Energy consumption and CO₂ emissions of the European glass industry. *Energy Policy*. 2011, **39**, 142–155.
2. Zier, M., Stenzel, P., Kotzur, L. & Stolten, D. A review of decarbonization options for the glass industry. *Energy Conversion and Management: X*. 2021, **10**, 100083.
3. 2018 UK greenhouse gas emissions, provisional figures [Internet]. UK Department for Business, Energy & Industrial Strategy. 2019 [cited 2020 Mar 30]. p. 46. Available from: https://assets.publishing.service.gov.uk/government/uploads/system/uploads/attachment_data/file/790626/2018-provisional-emissions-statistics-report.pdf
4. Industrial Decarbonisation & Energy Efficiency Roadmaps to 2050: Cross Sector Summary [Internet]. UK Department for Business, Innovation & Skills and Department Change, of Energy & Climate. 2015 [cited 2020 Mar 30]. p. 31. Available from: https://assets.publishing.service.gov.uk/government/uploads/system/uploads/attachment_data/file/419912/Cross_Sector_Summary_Report.pdf
5. de la Hera, G., Muñoz-Díaz, I., Cifrian, E., Vitorica, R., Gutierrez San Martin, O. & Viguri, J. R. Comparative Environmental Life Cycle Analysis of Stone Wool Production Using Traditional and Alternative Materials. *Waste and Biomass Valorization*. 2017, **8**, 1505–1520.
6. Schultz-Falk, V., Agersted, K., Jensen, P. A. & Solvang, M. Melting behaviour of raw materials and recycled stone wool waste. *J. Non-Cryst Solids*. 2018, **485**, 34–41.
7. Širok, B., Bizjan, B., Orbančić, A. & Bajcar, T. Mineral wool melt fiberization on a spinner wheel. *Chem. Eng. Res. Des.*, 2014, **92**, 80–90.
8. World Bioenergy Association. Global Bioenergy Statistics 2019 [Internet]. 2019. p. 58. Available from: <https://worldbioenergy.org/global-bioenergy-statistics>
9. Whitaker, J., Field, J. L., Bernacchi, C. J., Cerri, C. E. P., Ceulemans, R., Davies, C. A., Delucia, E. H., Donnison, I. S., McCalmont, J. P., Paustian, K., Rowe, R. L., Smith, P., Thornley, P and McNamara, N. P. Consensus, uncertainties and challenges for perennial bioenergy crops and land use. *GCB Bioenergy*, 2018, **10**, 150–64.
10. Vassilev, S. V., Baxter, D., Andersen, L. K. & Vassileva, C. G. An overview of the composition and application of biomass ash. Part 1. Phase-mineral and chemical composition and classification. *Fuel*, 2013, **105**, 40–76.
11. Trivedi, N. S., Mandavgane, S. A., Mehetre, S. & Kulkarni, B. D. Characterization and valorization of biomass ashes. *Environ. Sci. Pollut. Res.*, 2016, **23**, 20243–20256.
12. Lamers, F., Cremers, M., Matschegg, D., Schmidl, C., Hannam, K., Hazlett, P., Madrali, S., Primdal Dam, B., Roberto, R., Mager, R., Davidsson, K., Bech, N., Feuerborn, H.-J. & Saraber, A. Options for increased use of ash from biomass combustion and co-firing. *IEA Bioenergy*, 2018, 1–61.
13. Srisittipokakun, N., Kirdsiri, K., Ruangtaweep, Y. & Kaewkhao, J. Utilization of Pennisetum purpureum ash for use in glass material. *Adv. Mater. Res.*, 2013, **770**, 84–87.
14. Tan, Z. & Lagerkvist, A. Phosphorus recovery from the biomass ash: A review. *Renew. Sustain. Energy. Rev.*, 2011, **15**, 3588–3602.
15. Tosti, L., van Zomeren, A., Pels, J. R., Comans, R. N. J. Technical and environmental performance of lower carbon footprint cement mortars containing biomass fly ash as a secondary cementitious material. *Resour. Conserv. Recycl.*, 2018, **134**, 25–33.
16. Vassilev, S. V., Baxter, D., Andersen, L. K. & Vassileva, C. G. An overview of the composition and application of biomass ash.: Part 2. Potential utilisation, technological

- and ecological advantages and challenges. *Fuel.*, 2013, **105**, 19–39.
17. Melotti, R., Santagata, E., Bassani, M., Salvo, M. & Rizzo, S. A preliminary investigation into the physical and chemical properties of biomass ashes used as aggregate fillers for bituminous mixtures. *Waste Manag.*, 2013, **33**, 1906–1917.
 18. Kemp, V., McDonald, A., Brock, F. & Shortland, A. J. LA-ICP-MS analysis of Late Bronze Age blue glass beads from Gurob, Egypt. *Archaeometry.*, 2020, **62**, 42–53.
 19. Rehren, T. A review of factors affecting the composition of early Egyptian glasses and faience: alkali and alkali earth oxides. *J. Archaeol. Sci.*, 2008, **35**, 1345–1354.
 20. Schibille, N., Gratuze, B., Ollivier, E. & Blondeau, É. Chronology of early Islamic glass compositions from Egypt. *J. Archaeol. Sci.*, 2019, **104**, 10–18.
 21. Shortland, A. J. & Tite, M. S. Raw materials of glass from Amarna and implications for the origins of Egyptian glass. *Archaeometry.*, 2000, **42**, 141–151.
 22. Henderson, J., An, J. & Ma, H. The Archaeometry and Archaeology of Ancient Chinese Glass: a Review. *Archaeometry.*, 2018, **60**, 88–104.
 23. Yin, M., Rehren, T. & Zheng, J. The earliest high-fired glazed ceramics in China: The composition of the proto-porcelain from Zhejiang during the Shang and Zhou periods (c. 1700-221 BC). *J. Archaeol. Sci.* 2011, **38**, 2352–2365.
 24. Angelini, I., Artioli, G., Bellintani, P., Diella, V., Gemmi, M., Polla, A. & Rossi, A. Chemical analyses of Bronze Age glasses from Frattesina di Rovigo, Northern Italy. *J. Archaeol. Sci.*, 2004, **31**, 1175–1184.
 25. De Juan Ares, J., Calderón, N. F., Muñiz López, I., García Álvarez-Busto, A. & Schibille, N. Islamic soda-ash glasses in the Christian kingdoms of Asturias and León (Spain). *J. Archaeol. Sci. Reports*, 2018, **22**, 257–263.
 26. Rehren, T. & Freestone, I. C. Ancient glass: From kaleidoscope to crystal ball. *J. Archaeol. Sci.*, 2015, **56**, 233–241.
 27. Van Wersch, L., Loisel, C., Mathis, F., Strivay, D. & Bully, S. Analyses of Early Medieval Stained Window Glass From the Monastery of Baume-Les-Messieurs (Jura, France). *Archaeometry*, 2016, **58**, 930–946.
 28. Wedepohl, K. H. Carolingian glass from Staré Město- Sady (Moravia, Czech Republic). *J. Glass. Stud.*, 2012, **54**, 93–95.
 29. Kato, N., Nakai, I. & Shindo, Y. Transitions in Islamic plant-ash glass vessels: On-site chemical analyses conducted at the Raya/al-Tur area on the Sinai Peninsula in Egypt. *J. Archaeol. Sci.*, 2010, **37**, 1381–1395.
 30. Meek, A., Henderson, J. & Evans, J. Isotope analysis of English forest glass from the Weald and Staffordshire. *J. Anal. At. Spectrom.*, 2012, **27**, 786–795.
 31. Schalm, O., Caluwé, D., Wouters, H., Janssens, K., Verhaeghe, F. & Pieters, M. Chemical composition and deterioration of glass excavated in the 15th-16th century fishermen town of Raversijde (Belgium). *Spectrochim. Acta - Part B At. Spectrosc.*, 2004, **59**, 1647–1656.
 32. Wedepohl, K. H. & Simon, K. The chemical composition of medieval wood ash glass from Central Europe. *Chemie der Erde*, 2010, **70**, 89–97.
 33. Nakamura, K., Kitasato, Y., Takahashi, T. & Sanbongi, K. A Study on Manufacture of Mineral Wool from Pulverized Coal Burnt Ashes. *J. Soc. Mater. Sci. Japan*, 1969, **18**, 554–560.
 34. Manz, O. E. Utilization of By-Products from Western Coal Combustion in the Manufacture of Mineral Wool and Other Ceramic Materials. *Cem. Concr. Res.*, 1984, **14**, 513–520.
 35. Peacey, J. G. & Pelletier, A. Mineral wool production from copper reverberatory slag. *Can. Metall. Q.*, 1981, **20**, 241–245.
 36. Wang, W., Dai, S., Zhou, L., Zhang, T., Tian, W. & Xu, J. Effect of B₂O₃ on the

- properties of ferronickel melt and mineral wool. *Ceram. Int.*, 2020, **46**, 13460–13465.
37. Smedskjaer, M. M., Solvang, M. & Yue, Y. Crystallisation behaviour and high-temperature stability of stone wool fibres. *J. Eur. Ceram. Soc.*, 2010, **30**, 1287–1295.
 38. Moesgaard, M., Pedersen, H. D., Yue, Y. Z. & Nielsen, E. R. Crystallization in stone wool fibres. *J. Non-Cryst. Solids*. 2007, **353**, 1101–1108.
 39. Giles, H. L., Hurley, P. W. & Webster, H. W. M. Simple approach to the analysis of oxides, silicates and carbonates using x-ray fluorescence spectrometry. *X-Ray Spectrom.*, 1995, **24**, 205–218.
 40. Bell, A. M. T., Backhouse, D. J., Deng, W., Eales, J. D., Kilinc, E., Love, K., Rautiyal, P., Rigby, J. C., Stone, A. H., Vaishnav, S., Wie-Addo, G & Bingham, P. A. X-ray Fluorescence Analysis of Feldspars and Silicate Glass: Effects of Melting Time on Fused Bead Consistency and Volatilisation. *Minerals*, 2020, **10**, 442.
 41. Shuker, R. & Gammon, R. W. Raman-scattering selection-rule breaking and the density of states in amorphous materials. *Phys. Rev. Lett.*, 1970, **25**, 222–225.
 42. Galeener, F. L. & Sen, P. N. Theory for the first-order vibrational spectra of disordered solids. *Phys. Rev. B.*, 1978, **17**, 1928–1933.
 43. Le Losq, C., Neuville, D. R., Florian, P., Henderson, G. S. & Massiot, D. The role of Al³⁺ on rheology and structural changes in sodium silicate and aluminosilicate glasses and melts. *Geochim. Cosmochim. Acta*, 2014, **126**, 495–517.
 44. Long, D. A. Raman Spectroscopy. McGraw-Hill, New York, 1977, p. 276.
 45. Rancourt D. Recoil Mossbauer Spectral Analysis Software [Internet]. Ottawa: Intelligent Scientific Applications, Inc.; 1998. Available from: <http://www.isapp.ca/isarecoil.html>
 46. Dyar, M. D. A review of Mössbauer data on inorganic glasses: the effects of composition on iron valency and coordination. *Am. Mineral.*, 1985, **70**, 304–316.
 47. Burkhard, D. J. M. Iron-bearing silicate glasses at ambient conditions. *J. Non-Cryst. Solids*, 2000, **275**, 175–188.
 48. Kurkjian, C. R. Mössbauer spectroscopy in inorganic glasses. *J. Non-Cryst. Solids*, 1970, **3**, 157–194.
 49. Duchesne, M. A., Bronsch, A. M., Hughes, R. W. & Masset, P. J. Slag viscosity modeling toolbox. *Fuel*, 2013, **114**, 38–43.
 50. Vargas, S., Frandsen, F. J. & Dam-Johansen, K. Rheological properties of high-temperature melts of coal ashes and other silicates. *Prog. Energy Combust. Sci.*, 2001, **27**, 237–429.
 51. Watt, J. D. & Fereday, F. The flow properties of slag formed from the ashes of British coals. Part I. Viscosity of homogeneous liquid slag in relation to slag composition. *J. Inst. Fuel*, 1969, **42**, 99–103.
 52. Shaw, H. R. Viscosities of magmatic silicate liquids; an empirical method of prediction. *Am. J. Sci.*, 1972, **272**, 870–893.
 53. Browning, G. J., Bryant, G. W., Hurst, H. J., Lucas, J. A. & Wall, T. F. An empirical method for the prediction of coal ash slag viscosity. *Energy and Fuels*, 2003, **17**, 731–737.
 54. Duchesne, M. A., MacChi, A., Lu, D. Y., Hughes, R. W., McCalden, D. & Anthony, E. J. Artificial neural network model to predict slag viscosity over a broad range of temperatures and slag compositions. *Fuel Process Technol.*, 2010, **91**, 831–836.
 55. Deshkar, A., Ahmadzadeh, M., Scrimshire, A., Han, E., Bingham, P. A., Guillen, D., McCloy J. & Goel, A. Crystallization behavior of iron- and boron-containing nepheline (Na₂O·Al₂O₃·2SiO₂) based model high-level nuclear waste glasses. *J. Am. Ceram. Soc.*, 2019, **102**, 1101–1121.
 56. Bingham, P. A., Parker, J. M., Searle, T., Williams, J. M. & Smith, I. Novel structural

- behaviour of iron in alkali-alkaline-earth-silica glasses. *C. R. Chim.*, 2002, **5**, 787–796.
57. Bingham, P. A., Forder, S. D., Hand, R. J. & Lavaysierre, A. Mössbauer studies of phosphate glasses for the immobilisation of toxic and nuclear wastes. *Hyperfine Interact.*, 2005, **165**, 135–140.
 58. Dunaeva, E. S., Uspenskaya, I. A., Pokholok, K. V., Minin, V. V., Efimov, N. N., Ugolkova, E. A. & Brunet, E. Coordination and RedOx ratio of iron in sodium-silicate glasses. *J. Non-Cryst. Solids*, 2012, **358**, 3089–3095.
 59. Dyar, M. D., Agresti, D. G., Schaefer, M. W., Grant, C. A. & Sklute, E. C. Mössbauer Spectroscopy of Earth and Planetary Materials. *Annu. Rev. Earth Planet. Sci.*, 2006, **34**, 83–125.
 60. Ferreira, N. M., Kovalevsky, A. V., Valente, M. A., Sobolev, N. A., Waerenborgh, J. C., Costa, F. M. & Frade, J. R. Iron incorporation into magnesium aluminosilicate glass network under fast laser floating zone processing. *Ceram. Int.*, 2016, **42**, 2693–2698.
 61. Di Genova, D., Morgavi, D., Hess, K. U., Neuville, D. R., Borovkov, N., Perugini, D. & Dingwell, D. B. Approximate chemical analysis of volcanic glasses using Raman spectroscopy. *J. Raman Spectrosc.*, 2015, **46**, 1235–1244.
 62. Di Genova, D., Hess, K. U., Chevrel, M. O. & Dingwell, D. B. Models for the estimation of Fe³⁺/Fetot ratio in terrestrial and extraterrestrial alkali- and iron-rich silicate glasses using Raman spectroscopy. *Am. Mineral.*, 2016, **101**, 943–952.
 63. Schiavi, F., Bolfan-Casanova, N., Withers, A. C., Médard, E., Laumonier, M., Laporte, D., Flaherty, T. & Gómez-Ulla, A. Water quantification in silicate glasses by Raman spectroscopy: Correcting for the effects of confocality, density and ferric iron. *Chem. Geol.*, 2018, **483**, 312–331.
 64. Tarragó, M., Esteves, H., Garcia-Valles, M., Martínez, S. & Neuville, D. R. Effect of Ca in P-doped basaltic glass-ceramics: Application to waste inertization. *Mater. Lett.*, 2018, **220**, 266–268.
 65. Tarragó, M., Garcia-Valles, M., Martínez, S., Neuville, D. R. Phosphorus solubility in basaltic glass: Limitations for phosphorus immobilization in glass and glass-ceramics. *J. Environ. Manage.*, 2018, **220**, 54–64.
 66. Neuville, D. R. & Mysen, B. O. Role of aluminium in the silicate network: In situ, high-temperature study of glasses and melts on the join SiO₂-NaAlO₂. *Geochim. Cosmochim. Acta*. 1996, **60**, 1727–1737.
 67. White, W. B. & Minser, D. G. Raman spectra and structure of natural glasses. *J. Non-Cryst. Solids*. 1984, **67**, 45–59.
 68. Gutnikov, S. I., Manylov, M. S. & Lazoryak, B. I. Crystallization and thermal stability of the p-doped basaltic glass fibers. *Minerals*, 2019, **9**.
 69. Yadav, A. K. & Singh, P. A review of the structures of oxide glasses by Raman spectroscopy. *RSC Adv.*, 2015, **5**, 67583–67609.
 70. le Losq, C., Berry, A. J., Kendrick, M. A., Neuville, D. R. & O'Neill, H. S. C. Determination of the oxidation state of iron in Mid-Ocean Ridge basalt glasses by Raman spectroscopy. *Am. Mineral.*, 2019, **104**, 1032–1042.
 71. Lakatos, B., Johansson, T. & Simmingskold, L. G. Viscosity temperature relations in the glass system SiO₂-Al₂O₃-Na₂O-K₂O-CaO-MgO. *Glass Technol.*, 1972, **13**, 88–95.
 72. Lakatos, B., Johansson, T. & Simmingskold, L. G. The effect of some components on the viscosity of glass. *Glastek Tidskr.*, 1972, **27**, 25–28.
 73. Lakatos, B., Johansson, T. & Simmingskold, L. G. Viscosity temperature relations in glasses composed of SiO₂-Al₂O₃-Na₂O-K₂O-Li₂O-CaO-MgO-BaO-ZnO-PbO-B₂O₃. *Glastek Tidskr.*, 1976, **31**, 51–54.
 74. Mauro, J. C., Yue, Y., Ellison, A. J., Gupta, P. K. & Allan, D. C. Viscosity of glass-

- forming liquids. *Proc. Natl. Acad. Sci.*, 2009, **106**, 19780–19784.
75. Lund, M. D., Yue, Y. & Lybye, D. Impact of the oxidation state of iron on the tensile strength of stone wool fibres. *Glass Technol.: Eur. J. Glass Sci. Technol. Part A*, 2010, **51**, 97–102.
 76. Yue, Y., Korsgaard, M., Kirkegaard, L. F. & Heide, G. Formation of a nanocrystalline layer on the surface of stone wool fibers. *J. Am. Ceram. Soc.*, 2009, **92**, 62–67.
 77. Bingham, P. A. Design of New Energy-Friendly Compositions. In: Wallenberger FT, Bingham PA, editors. *Fiberglass and Glass Technology - Energy-Friendly Compositions and Applications*. Springer US, New York, 2010, p. 267 – 351.
 78. Leth-Miller, R., Jensen, A. D., Jensen, J., Glarborg, P., Jensen, L. M., Hansen, P. B. & Jørgensen, S. B. Comparative study of reactivity to CO₂ of cokes used in stone wool production. *Fuel Process Technol.*, 2005, **86**, 551–563.
 79. Gong, K. & White, C. E. Impact of chemical variability of ground granulated blast-furnace slag on the phase formation in alkali-activated slag pastes. *Cem. Concr. Res.*, 2016, **89**, 310–319.
 80. Blotevogel, S., Ehrenberg, A., Steger, L., Doussang, L., Kaknics, J., Patapy, C. & Cyr, M. Ability of the R3 test to evaluate differences in early age reactivity of 16 industrial ground granulated blast furnace slags (GGBS). *Cem. Concr. Res.*, 2020, **130**, 105998–106010.
 81. Oberteuffer, J. A. Magnetic Separation: A Review of Principles, Devices, and Applications, *IEEE Trans. Magn.*, 1974, **10**, 223–238.
 82. Bavdaž, G. & Kocijan, J. Fuzzy controller for cement raw material blending. *Trans. Inst. Meas. Control*, 2007, **29**, 17–34.
 83. Krijgsman, R. & Marsidi, M. Decarbonisation options for the Dutch stone wool industry. *PBL Netherlands Environmental Assessment Agency*, 2019. Available online at: https://www.pbl.nl/sites/default/files/downloads/pbl-2019-decarbonisation-options-for-the-dutch-stone-wool-industry_3722.pdf, accessed 22nd October 2021.
 84. Schultz-Falk, V. Waste recycling in an integrated melting furnace for stone wool production, PhD thesis, 2020. Technical University of Denmark. Available online at: https://backend.orbit.dtu.dk/ws/portalfiles/portal/239705051/PhD_Thesis_Vickie_Schultz_Falk.pdf, accessed 22nd October 2021.

Figure/Table Caption List

Figure 1. X-Ray diffractograms for each mineral wool sample. The diffractograms have been artificially separated along the y-axis in order to aid visual comparison.

Figure 2. Long-corrected Raman spectra for each mineral wool sample. The spectra have been artificially separated along the y-axis in order to aid visual comparison.

Figure 3. Difference plot of the Long-corrected Raman spectra for each mineral wool sample compared to the benchmark MW.

Figure 4. Fitted room temperature ^{57}Fe Mössbauer spectra of, in order from top to bottom, MW, MW-C, FA-10, BA-10. Centre shifts are relative to α -Fe foil.

Table 1. Batch compositions of mineral wool glass samples, in grammes.

Table 2. XRF-determined compositions of raw materials used in mineral wool sample production. All values in wt. %. Uncertainties are shown in brackets.

Table 3. XRF-determined compositions of Biomass Fly Ash and Biomass Bottom Ash, plus carbon content from combustion analysis. All values in wt. %. Uncertainties are shown in brackets.

Table 4. Compositions of mineral wool glass samples, in weight percent, as determined by XRF spectroscopy, with measured densities (determined by the Archimedes Method) and molar volumes. Uncertainties are shown in brackets.

Table 5. Mean and σ values for the major oxides (> 1 wt.%) in the mineral wool samples.

Table 6. Fitting parameters for the Mössbauer spectra shown in Figure 4.

Table 7. Batched CO_2 levels for each sample.

Table 8. Thermal expansion coefficient (α), dilatometric softening point (T_d) and glass transition temperature (T_g) values for the MW samples, derived from dilatometric analysis.

Table 9. Melting and fibre-forming temperatures extracted from viscosity modelling of each sample using the SVP tool developed by Duchesne *et al.*⁴⁸ Uncertainties are shown in

brackets.

Table 10. Log (η / dPa·s) values for MW determined at 100 °C intervals by each viscosity model. Uncertainties (AALE) are shown in brackets.

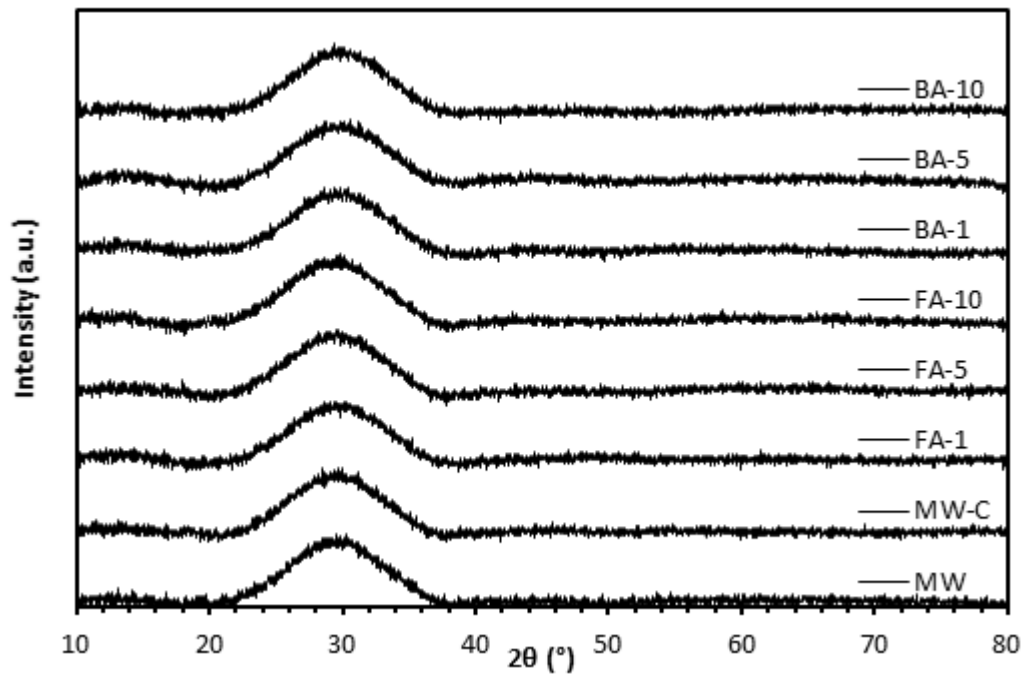


Figure 1. X-Ray diffractograms for each mineral wool sample. The diffractograms have been artificially separated along the y-axis in order to aid visual comparison.

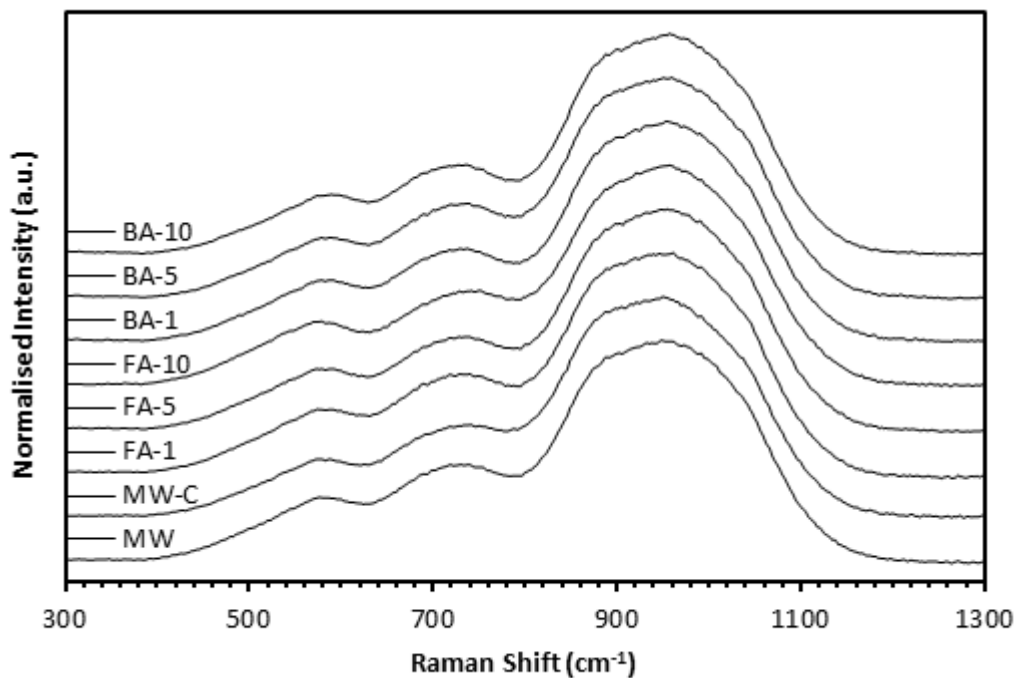


Figure 2. Long-corrected Raman spectra for each mineral wool sample. The spectra have been artificially separated along the y-axis in order to aid visual comparison.

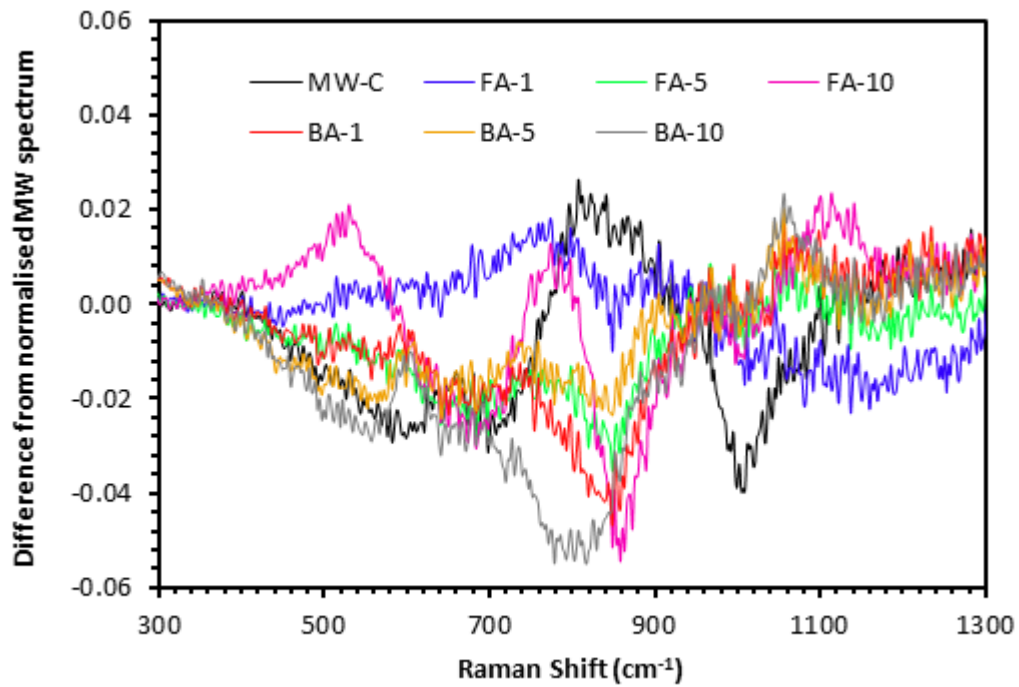


Figure 3. Difference plot of the Long-corrected Raman spectra for each mineral wool sample compared to the benchmark MW.

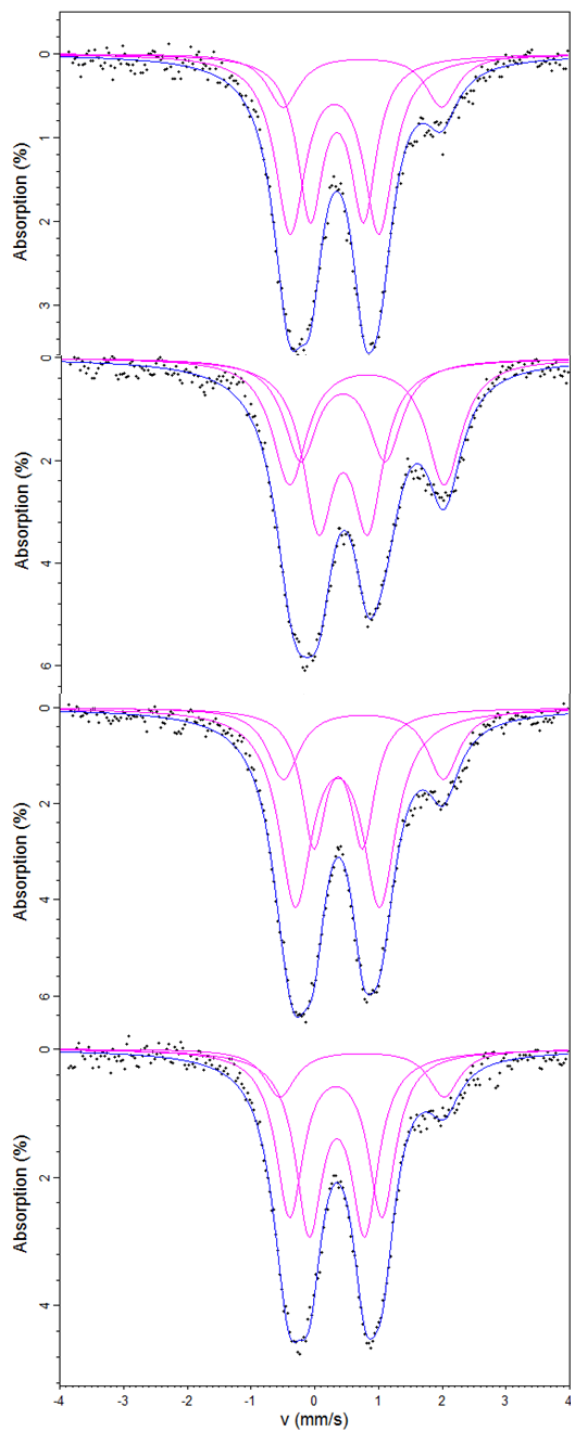


Figure 4. Fitted room temperature ^{57}Fe Mössbauer spectra of, in order from top to bottom, MW, MW-C, FA-10, BA-10. Centre shifts are relative to α -Fe foil.

Table 1. Batch compositions of mineral wool glass samples, in grammes.

Sample	MW	MW-C	FA-1	FA-5	FA-10	BA-1	BA-5	BA-10
Basalt	30.00	28.50	29.68	28.38	26.75	29.47	27.30	24.59
Dolomite	9.00	8.55	8.87	8.35	7.71	9.31	10.59	12.18
Blast Furnace Slag	3.50	3.33	3.56	3.88	4.27	3.20	2.09	0.70
Steel Slag	7.50	7.13	7.39	6.89	6.27	7.52	7.53	7.54
Coke	0.00	2.50	0.00	0.00	0.00	0.00	0.00	0.00
BFA	0.00	0.00	0.50	2.50	5.00	0.00	0.00	0.00
BBA	0.00	0.00	0.00	0.00	0.00	0.50	2.50	5.00
Total	50.00	50.01	50.00	50.00	50.00	50.00	50.01	50.01

Table 2. XRF-determined compositions of raw materials used in mineral wool sample production. All values in wt. %. Uncertainties are shown in brackets.<l.d., below limit of detection

	Basalt	Blast Furnace Slag	Steel Slag	Dolomite
Na₂O	3.65 (0.09)	0.35 (0.02)	<l.d. (0.00)	<l.d. (0.00)
MgO	5.38 (0.10)	7.19 (0.12)	3.52 (0.08)	34.23 (0.21)
Al₂O₃	17.67 (0.17)	11.32 (0.16)	1.03 (0.06)	0.37 (0.02)
SiO₂	55.11 (0.25)	36.07 (0.21)	12.47 (0.16)	0.47 (0.03)
P₂O₅	0.14 (0.01)	<l.d. (0.00)	1.26 (0.14)	<l.d. (0.00)
SO₃	0.01 (0.00)	0.94 (0.05)	0.17 (0.01)	<l.d. (0.00)
K₂O	0.37 (0.02)	0.91 (0.05)	0.02 (0.00)	0.10 (0.01)
CaO	6.84 (0.12)	40.41 (0.22)	38.48 (0.21)	63.95 (0.27)
TiO₂	1.00 (0.06)	1.28 (0.06)	0.63 (0.04)	0.10 (0.01)
V₂O₅	<l.d. (0.00)	<l.d. (0.00)	0.59 (0.03)	<l.d. (0.00)
Cr₂O₃	<l.d. (0.00)	<l.d. (0.00)	0.32 (0.02)	<l.d. (0.00)
MnO₂	0.18 (0.01)	0.92 (0.05)	5.47 (0.10)	0.17 (0.01)
Fe₂O₃	9.54 (0.14)	0.30 (0.02)	35.90 (0.21)	0.61 (0.06)
ZnO	0.03 (0.00)	0.02 (0.00)	<l.d. (0.00)	<l.d. (0.00)
SrO	0.03 (0.00)	0.08 (0.01)	0.05 (0.01)	<l.d. (0.00)
BaO	0.04 (0.00)	0.14 (0.01)	0.01 (0.00)	<l.d. (0.00)
HfO₂	<l.d. (0.00)	<l.d. (0.00)	0.05 (0.01)	<l.d. (0.00)
ZrO₂	0.02 (0.00)	0.07 (0.01)	0.04 (0.00)	<l.d. (0.00)
Total	100.00	100.00	100.00	100.00

Table 3. XRF-determined compositions of Biomass Fly Ash and Biomass Bottom Ash, plus carbon content from combustion analysis. All values in wt. %. Uncertainties are shown in brackets. <1.d., below limit of detection

	Biomass Fly Ash	Biomass Bottom Ash
Na₂O	1.10 (0.06)	2.09 (0.07)
MgO	2.22 (0.07)	1.52 (0.06)
Al₂O₃	16.96 (0.17)	8.32 (0.13)
SiO₂	37.99 (0.21)	65.32 (0.27)
P₂O₅	1.61 (0.07)	0.69 (0.04)
SO₃	3.18 (0.08)	0.20 (0.02)
Cl	0.21 (0.02)	0.06 (0.01)
K₂O	8.50 (0.13)	3.64 (0.09)
CaO	15.45 (0.17)	12.45 (0.16)
TiO₂	1.15 (0.06)	<1.d. (0.00)
V₂O₅	<1.d. (0.00)	0.02 (0.00)
Cr₂O₃	0.05 (0.01)	0.04 (0.00)
MnO₂	0.51 (0.03)	0.20 (0.02)
Fe₂O₃	10.71 (0.16)	3.93 (0.09)
NiO	<1.d. (0.00)	0.21 (0.02)
CuO	<1.d. (0.00)	0.98 (0.05)
ZnO	0.01 (0.00)	0.01 (0.00)
SrO	0.14 (0.01)	0.04 (0.00)
ZrO₂	<1.d. (0.00)	0.05 (0.01)
BaO	0.22 (0.02)	0.16 (0.01)
PbO	<1.d. (0.00)	0.06 (0.01)

Total	100·00	100·00
Carbon	6·26 (0·11)	0·24 (0·02)

Table 4. Compositions of mineral wool glass samples, in weight percent, as determined by XRF spectroscopy, with measured densities (determined by the Archimedes Method) and molar volumes. Uncertainties are shown in brackets. <l.d., below limit of detection

	MW	MW-C	FA-1	FA-5	FA-10	BA-1	BA-5	BA-10
Na₂O	2.04 (0.07)	2.06 (0.07)	2.07 (0.07)	2.02 (0.07)	1.97 (0.07)	2.13 (0.07)	2.06 (0.07)	2.07 (0.07)
MgO	7.25 (0.12)	6.87 (0.12)	6.93 (0.12)	6.88 (0.12)	6.62 (0.12)	7.29 (0.12)	7.51 (0.12)	7.90 (0.13)
Al₂O₃	14.43 (0.17)	16.00 (0.17)	14.25 (0.17)	15.33 (0.17)	15.17 (0.17)	14.15 (0.17)	14.17 (0.17)	13.50 (0.16)
SiO₂	39.59 (0.22)	39.18 (0.22)	39.73 (0.22)	38.85 (0.22)	40.23 (0.22)	39.65 (0.22)	39.54 (0.22)	39.82 (0.22)
P₂O₅	0.32 (0.02)	0.32 (0.02)	0.37 (0.02)	0.32 (0.02)	0.40 (0.03)	0.33 (0.02)	0.33 (0.02)	0.33 (0.02)
SO₃	0.10 (0.01)	<l.d. (0.00)	0.10 (0.01)	0.09 (0.01)	0.04 (0.00)	0.09 (0.01)	0.07 (0.01)	0.02 (0.00)
K₂O	0.19 (0.01)	0.21 (0.02)	0.51 (0.03)	0.26 (0.02)	0.81 (0.05)	0.22 (0.02)	0.30 (0.02)	0.43 (0.03)
CaO	21.38 (0.18)	21.48 (0.18)	21.49 (0.18)	21.41 (0.18)	21.10 (0.18)	21.48 (0.18)	21.46 (0.18)	21.43 (0.18)
TiO₂	0.96 (0.05)	0.98 (0.05)	0.93 (0.05)	0.92 (0.05)	0.92 (0.05)	0.90 (0.05)	0.89 (0.05)	0.85 (0.05)
Cr₂O₃	0.06 (0.01)	0.05 (0.01)	0.05 (0.01)	0.05 (0.01)	0.05 (0.01)	0.06 (0.01)	0.06 (0.01)	0.06 (0.01)
MnO₂	1.28 (0.06)	1.31 (0.06)	1.27 (0.06)	1.30 (0.06)	1.16 (0.06)	1.29 (0.06)	1.28 (0.06)	1.29 (0.06)
Fe₂O₃	12.28 (0.16)	11.46 (0.16)	12.15 (0.16)	12.48 (0.16)	11.39 (0.16)	12.30 (0.16)	12.22 (0.16)	12.16 (0.16)
ZnO	0.02 (0.00)	<l.d. (0.00)	0.03 (0.00)	0.02 (0.00)	0.03 (0.00)	0.03 (0.00)	0.03 (0.00)	0.05 (0.01)
SrO	0.04 (0.00)	0.04 (0.00)	0.04 (0.00)	0.03 (0.00)	0.03 (0.00)	0.04 (0.00)	0.03 (0.00)	0.04 (0.00)
BaO	0.02 (0.00)	0.03 (0.00)	0.04 (0.00)	0.02 (0.00)	0.05 (0.01)	0.02 (0.00)	0.02 (0.00)	0.03 (0.00)
ZrO₂	0.03 (0.00)	0.03 (0.00)	0.04 (0.00)	0.03 (0.00)	0.03 (0.00)	0.02 (0.00)	0.02 (0.00)	0.02 (0.00)
Total	100.00	100.00	100.00	100.00	100.00	100.00	100.00	100.00
Density (g/cm³)	2.953 (0.0009)	2.939 (0.0002)	2.942 (0.0005)	2.943 (0.0003)	2.923 (0.0003)	2.957 (0.0006)	2.953 (0.0001)	2.956 (0.0015)
Molar Volume (cm³/mol)	22.30 (1.12)	22.23 (1.11)	22.43 (1.12)	22.52 (1.13)	22.57 (1.13)	22.24 (1.11)	22.24 (1.11)	22.11 (1.11)

Table 5. Mean and σ values for the major oxides (> 1wt.%) in the mineral wool samples.

	Na₂O	MgO	Al₂O₃	SiO₂	CaO	MnO₂	Fe₂O₃
Mean (wt.%)	2.05	7.16	14.62	39.57	21.40	1.27	12.05
σ (wt.%)	0.041	0.388	0.755	0.388	0.119	0.044	0.377
RSD	2.01	5.42	5.16	0.98	0.56	3.44	3.13

Table 6. Fitting parameters for the Mössbauer spectra shown in Figure 4.

	CS (mm s⁻¹) [+/- 0.02]	QS (mm s⁻¹) [+/- 0.02]	HWHM (mm s⁻¹) [+/- 0.02]	Area (%) [+/- 2]
MW				
Fe(III) Tet.	0.35	0.84	0.24	37
Fe(III) Oct.	0.31	1.39	0.29	48
Fe(II)	0.75	2.49	0.30	15
MW-C				
Fe(III) Tet.	0.43	0.77	0.29	39
Fe(III) Oct.	0.43	1.33	0.31	26
Fe(II)	0.80	2.43	0.33	35
MW-FA10				
Fe(III) Tet.	0.37	0.77	0.23	27
Fe(III) Oct.	0.36	1.32	0.32	54
Fe(II)	0.77	2.51	0.30	19
MW-BA10				
Fe(III) Tet.	0.35	0.87	0.26	44
Fe(III) Oct.	0.33	1.45	0.26	42
Fe(II)	0.74	2.58	0.30	14

Table 7. Estimated batched CO₂ levels for each sample.

	MW	FA-1	FA-5	FA-10	BA-1	BA-5	BA-10
Batched CO₂ (g)	5.40	5.33	5.01	4.63	5.59	6.36	7.31
CO₂ per Tonne Batch (kg)	108.0	106.5	100.2	92.6	111.8	127.1	146.2

Table 10. Log (η / dPa·s) values for sample MW determined at 100 °C intervals by each viscosity model. Uncertainties (AALE) are shown in brackets.

Temperature (°C)	Log (η / dPa·s)			
	S ² (0·27)	Watt-Fereday (0·33)	Shaw (0·55)	BBHLW (0·30)
1500	0·77	0·63	0·70	0·59
1400	1·20	0·93	0·98	0·94
1300	1·68	1·32	1·30	1·32
1200	2·23	1·82	1·66	1·76
1100	2·85	2·48	2·08	2·24
1000	3·57	3·39	2·56	2·79
900	4·42	4·69	3·12	3·42
800	5·43	6·63	3·79	4·14
700	6·64	9·73	4·59	4·99
600	8·13	15·11	5·58	5·98

Table 11. Summary of XRF-determined chemical composition data obtained on 17 samples taken across a 13-month period.

	Mean	Standard Deviation, σ	Relative Standard Deviation, %	Min.	Max.	Range	Absolute Variation (10 wt.% BFA)
Na ₂ O	0.88	0.14	15.94	0.67	1.16	0.49	0.05
MgO	2.55	0.16	6.10	2.21	2.90	0.69	0.07
Al ₂ O ₃	15.35	1.05	6.81	12.45	16.96	4.51	0.45
SiO ₂	34.07	2.12	6.23	29.09	38.16	9.07	0.91
P ₂ O ₅	1.94	0.19	10.02	1.60	2.38	0.78	0.08
SO ₃	3.74	0.84	22.59	2.14	5.53	3.39	0.34
Cl	0.27	0.08	29.72	0.14	0.46	0.32	0.03
K ₂ O	11.49	0.99	8.65	8.48	12.73	4.25	0.43
CaO	17.12	1.74	10.15	14.05	21.80	7.75	0.77
TiO ₂	1.12	0.04	3.85	1.04	1.20	0.16	0.02
V ₂ O ₅	0.03	0.03	95.62	0.00	0.08	0.08	0.01
Cr ₂ O ₃	0.05	0.01	12.38	0.04	0.07	0.02	0.00
MnO ₂	0.74	0.13	16.97	0.51	1.03	0.52	0.05
Fe ₂ O ₃	9.97	0.46	4.59	9.16	10.95	1.79	0.18
NiO	0.03	0.01	16.26	0.00	0.04	0.04	0.00
CuO	0.04	0.00	9.43	0.00	0.04	0.04	0.00
ZnO	0.18	0.02	13.25	0.01	0.21	0.20	0.02
Rb ₂ O	0.00	0.01	400.00	0.00	0.03	0.03	0.00

SrO	0.14	0.01	6.85	0.13	0.16	0.03	0.00
ZrO₂	0.04	0.00	10.62	0.00	0.05	0.05	0.00
BaO	0.23	0.02	7.52	0.20	0.26	0.06	0.01
PbO	0.03	0.01	42.28	0.00	0.05	0.05	0.01
